Dual responsive polymersomes as versatile, intelligent labeling system in biosensing

Jennifer Quinchia,[a] Andrés F. Cruz-Pacheco,[a] Daniel Ruiz-Molina,[b] Jahir Orozco[a]*

[a] Max Planck Tandem Group in Nanobioengineering, Institute of Chemistry, Faculty of Exact and Natural Sciences, University of Antioquia. Complejo Ruta N, Calle 67 No. 52-20, Medellín 050010, Colombia

[b] Catalan Institute of Nanoscience and Nanotechnology (ICN2), CSIC and BIST, Campus UAB, Bellaterra, Barcelona, 08193, Spain

*Corresponding author: grupo.tandemnanobioe@udea.edu.co[1]

ABSTRACT

The ability to manipulate artificial nanosystems is still one of the current challenges in developing multifunctional nanomaterials. Those based on the photochromic effect are particularly interesting because of structural and functional control by the transient activation/inactivation with high spatiotemporal resolution. To mimic the photocontrol of natural nanosystems, we developed the first photochromic polymersomes from the novel poly(ethylene-*alt*-maleic anhydride)-random-aminoazobenzene copolymer (PEMA-*r*-AAB) and its derivatives. Ultraviolet (UV)-triggered azobenzene (AZO) moieties' medium-dependent isomerization from non-polar *trans*- to polar *cis*-AZO controls polymersome's bilayer selective permeability. As a result, small hydrophilic molecules loaded inside polymersomes can be released according to the release profiles, while those outside the polymersome bilayer can eventually penetrate it. Remarkably, as a new look, cargo photorelease from the nanopolymersomes was studied

---

[1] **Abbreviation: b-DAbs:** biotinylated detection antibodies; **CAbs:** capture antibodies; **DS:** degree of substitution; **Fc-$V_{PEMA-AAB}$:** ferrocene-loaded $V_{PEMA-AAB}$; **HRP:** horseradish peroxidase; **HRP-$V_{PEMA-AAB}$:** horseradish peroxidase -loaded $V_{PEMA-AAB}$; **MB-$V_{PEMA-AAB}$:** Methylene blue-loaded $V_{PEMA-AAB}$; ***p*-AAB:** 4-aminoazobenzene; **PEMA:** poly(ethylene-*alt*-maleic anhydride); **PEMA-*r*-AAB:** random copolymer synthesized from PEMA and *p*-AAB; **PEMA-*r*-AAB-*r*-biotin,** ran- dom copolymer synthesized from PEMA, *p*-AAB and biotin; **polyHRP20–$V_{PEMA-AAB-biotin}$–MB:** $V_{PEMA-AAB-biotin}$– magnetic beads conjugate with strep-polyHRP20; **Pt@SC NPs:** nanoparticles of platinum stabilized with sodium citrate; **Pt-$V_{PEMA-AAB}$:** platinum nanoparticle-loaded $V_{PEMA-AAB}$; **$V_{PEMA-AAB}$:** polymersomes self-assembly from PEMA-*r*-AAB; **$V_{PEMA-AAB-biotin}$:** polymersomes self-assembly from PEMA-*r*-AAB-*r*-biotin.

in real-time by cyclic voltammetry (CV). Finally, as a proof-of-concept, horseradish peroxidase (HRP)-loaded polymersomes were assembled as an intelligent labeling system of an optical biosensor of interleukin-6 (IL-6). This synthesis route can be exploited with other photo-switching AZO derivatives, paving the way toward new AZO compound-based nanocarrier systems.

KEYWORDS: AZO compounds • Photochromism • Real-time cyclic voltammetry studies • Smart labeling system • Smart polymersome • UV-induced medium-dependent cargo release

1. Introduction

The ability to manipulate and control artificial nanosystems is a big challenge in nanotechnology and nanomedicine. In this context, the construction of manipulable and programmable artificial smart nanosystems requires the incorporation of stimuli-responsive moieties [1], for example, that enable their non-invasive spatiotemporal photochemical control [2–5]. The most well-studied and versatile method of photochemical control at the nanoscale is introducing photochromism into artificial nanosystems [6]. Photochromism is the photoinduced reversible chemical transformation of chemical species between two states [7,8]. Photochromism drives (nano)systems out-of-original state when photostimulated while returning to their original state when removing or changing the photostimulation source. It expands their potential to dynamic, reusable, and reprogrammable nanosystems. The photogenerated chemical species can be reversed to the initial species by either thermal relaxation or irradiation with ultraviolet (UV) or visible (vis) light [8].

Synthetic organic photochromes are attractive due to their capacity to switch in response to light stimulation. Particularly, AZO-derivative molecules incorporated into various nanosystems have shown a wide range of potential uses [9–11]. In general, irradiation of AZO derivatives with UV light induces the geometric isomerization around the N=N double bond, converting *trans*- to *cis*-isomer. Significant changes in structural geometry, dipole moment, and absorption spectra typically accompany these two states' interconversion. While *trans*-AZO has a planar structure of 9 Å length with nearly zero dipole moment, *cis*-AZO is less flat (6 Å length) and has a more significant dipole moment (3 D) [12–14]. Depending on the AZO-based nanosystem architecture, the photoinduced chemical transformation at the molecular

scale can eventually originate a series of macroscopic effects, including the collective rearrangement of the AZO moieties and the structural reconfiguration of the hosting nanosystem at increasing spatial scales [14].

Among different types of artificial nanosystems, polymersomes can encapsulate active hydrophilic and hydrophobic cargoes in their aqueous core and hydrophobic bilayer membrane, thus offering great structural and functional versatility [4,15,16]. Based on the geometry and dipole moment differences between *trans*- and *cis*-isomers, polymersomes self-assembled from AZO-based copolymers exhibit photoresponse disassembly, re-assembly, or other morphological changes [17,18]. According to the structural reconfiguration of AZO-based polymersomes that occurred by photostimulation, the ongoing cargo monitoring could offer additional information about the release process. Electrochemical measurements are desirable in this context because electrical signals can be easily generated during stimulus-induced cargo release without needing robust, specialized, and complex equipment. Therefore, it offers an attractive alternative to spectrophotometry, fluorescence, or High-Performance Liquid Chromatography (HPLC) detection. For example, electrochemical assays have continuously monitored cargo release from lipid-based and electroresponsive drug delivery systems (DDSs) [19–23]. Other works have integrated electrochemical systems into studying stable films' photochemical properties and pH sensitivity [24]. However, no work has reported their application to study the in situ light-induced cargo release.

This work faces two significant challenges in developing multifunctional photosensitive polymersomes. The first focused on the rapid and easy obtention of photosensitive copolymers and their self-assembly in highly dispersed polymersomes, and the second on the real-time electrochemical study of photorelease. Therefore, it develops well-defined photosensitive polymersomes self-assembled from two novel AZO-based photochromic amphiphilic random copolymers by nanoprecipitation. PEMA-*r*-AAB and PEMA-*r*-AAB-*r*-biotin copolymers were synthesized by the one-step nucleophilic substitution of amine-containing hydrophobic (4-aminoazobenzene, *p*-AAB) and hydrophilic (amine-PEG3-biotin, biotin) moieties onto a poly(ethylene-*alt*-maleic anhydride) (PEMA) backbone like the incorporation of amine-containing azo dyes onto copolymers featuring cyclic anhydride functionality [25,26]. To our knowledge, PEMA has not been modified with photosensitive hydrophobic molecules

to obtain amphiphilic photosensitive random copolymers. Besides, AZO-based random copolymers have been less used to self-assemble polymersomes than conventional block copolymers because their dispersity in molecular weight usually leads to polydisperse assembled structures [17]. Therefore, this work demonstrates the self-assembly of well-organized nanopolymersomes from highly dispersed PEMA-*r*-AAB and PEMA-*r*-AAB-*r*-biotin copolymers. The AZO moieties' medium-dependent photochemical *trans*-to-*cis* isomerization worked as molecular switches to change polymersomes' bilayer permeability and selectively control hydrophilic cargo uptake and release (Scheme 1).

In a novel way, UV-induced cargo release was studied in real time using cyclic voltammetry (CV). Finally, as a proof-of-concept motivated by polymersome capabilities in analytical sciences, this work also reports on assembling horseradish peroxide (HRP)-loaded smart polymersomes as a novel labeling system in the optical biosensing of interleukin-6 (IL-6), studying the determinant factors affecting their successful incorporation into an enhanced immunosorbent-like assay.

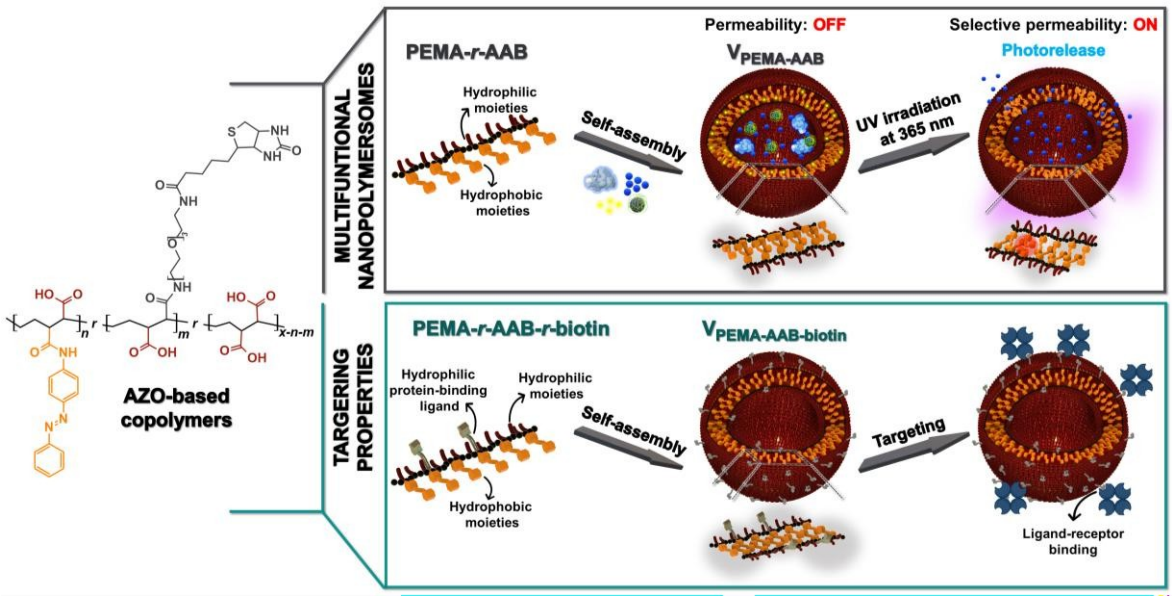

Scheme 1. Photosensitive polymersomes as versatile smart nanocarriers. Photochromic polymersomes self-assembled from the novel AZO-based copolymers, PEMA-*r*-AAB and PEMA-*r*-AAB-*r*-biotin with selective permeability for off-on site-specific cargo delivery applications. The ability of AZO moieties to isomerize from a nonpolar *trans*- to polar *cis*-AZO upon UV irradiation controls the polymersome's bilayer permeability.

2. Materials and Methods

The detailed procedure for amphiphilic photosensitive random copolymers synthesis, stability tests, UV-induced polymersomes behavior, hydrophobic and hydrophilic cargo encapsulation, UV-induced cargo release, and assembly of sandwich-type immunoassay is described in the supporting information (SI). In addition, the reagents and solutions used in all the tests are also in the SI.

3. Results and discussion

3.1. Amphiphilic photosensitive random copolymers: design and synthesis

The designed AZO-based copolymers were synthesized by the one-step nucleophilic substitution of amine-containing molecules in the PEMA backbone (Scheme S1), thanks to the few unique features of PEMA and their counterparts [27]. First, PEMA is highly reactive due to its two structural units, i.e., succinic anhydride and ethylene. While succinic anhydride is per se, highly reactive via nucleophilic substitution [28], ethylene groups between neighboring anhydride rings minimize steric restraints and boost cyclic anhydride reactivity. As a result, coupling agents are not required, simplifying the purification process and increasing reaction efficiency by up to 100 %. Second, the availability of several succinic anhydrides per polymer chain allows the chemical linkage of multiple side moieties with different chemical functionalities.

Herein, we synthesized PEMA-*r*-AAB and PEMA-*r*-AAB-*r*-biotin copolymers by modification of PEMA with *p*-AAB as photoswitchable and hydrophobic moieties and biotin as a streptavidin-binding ligand and hydrophilic moieties (Scheme S1). These modifications were confirmed by ^{1}H-NMR (Figure S1) and FTIR (Figure S2) [28–30]. The degree of substitution (DS) of *p*-AAB moieties in PEMA-*r*-AAB and PEMA-*r*-AAB-*r*-biotin was calculated based on the ratio of the integrated areas of aromatic protons to ethylene protons on the copolymer backbone. It was possible because the proton nuclear magnetic resonance (^{1}H-NMR) spectrum of PEMA (Figure S1C) demonstrated that the ethylene-to-succinic anhydride ratio is approximately 1:1. The DS of *p*-AAB was 53.5 % and 48.1 % for PEMA-*r*-AAB and PEMA-*r*-AAB-*r*-biotin, respectively, indicating that about half of the anhydride groups on PEMA were substituted with *p*-AAB. The low reaction efficiency is associated with the nucleophilicity of the *p*-AAB compound. Its protonated resonance structure forms a non-nucleophilic

ammonium compound. Besides, after the substitution reaction, ammonium *p*-AAB can stabilize the resultant conjugate base (carboxylate) via electrostatic interactions. The DS of biotin in PEMA-*r*-AAB-*r*-biotin was 3.8 %. Therefore, *p*-AAB and biotin randomly reacted with succinic anhydride units to produce ethyl-(N-(*p*-AAB)-succinamic acid), ethyl-(N-(biotin)-succinamic acid), and ethyl-(succinic acid) units. Each of these structural units is randomly distributed along the polymeric backbone, resulting in polydisperse copolymers, both in the molecular weight and density of the side moieties.

These novel copolymers were thermally less stable than PEMA under an inert atmosphere (Figures S3A-B, Table S1). PEMA displayed stability up to 250 °C. After this point, the degradation of the cyclic anhydride and the residual PEMA backbone was responsible for two thermal decomposition events [31]. The thermograms for PEMA-*r*-AAB and PEMA-*r*-AAB-*r*-biotin revealed similar weight loss in three steps. The evolution of moisture is connected to the initial step. The formation of carbon oxides (CO_x), the breakdown of side moieties, and the remaining PEMA backbone may all contribute to the second and third stages of weight loss [31].

3.2. Self-assembly of PEMA-*r*-AAB and PEMA-*r*-AAB-*r*-biotin polymersomes and stability studies

Polymersome or polymeric vesicles (V) of PEMA-*r*-AAB and PEMA-*r*-AAB-*r*-biotin were successfully self-assembled by the simple nanoprecipitation method, named $V_{PEMA\text{-}AAB}$ and $V_{PEMA\text{-}AAB\text{-}biotin}$, respectively. Dynamic light scattering (DLS) analysis of the PEMA-*r*-AAB copolymer's assembly, shown in Figure 1A and Table 1, revealed the formation of low disperse particles with monomodal size distribution and a smoothed single exponential decay autocorrelation function with an optimal signal-to-noise ratio (Y-intercept > 0.9). From static light scattering (SLS) analysis, the variation of scattered light intensity at different angles (Guinier plot) was exploited to calculate the radius of gyration (R_g) of PEMA-*r*-AAB copolymer's assembly (Figure 1B, the detail for the calculation of R_g is provided in the materials and methods section). The R_g of PEMA-*r*-AAB copolymer's assembly calculated by the SLS data was 65.1 nm. The radius of gyration and the hydrodynamic radius (R_g/R_H) ratio was further employed to analyze the morphology of the PEMA-*r*-AAB copolymer's assembly. The R_g/R_H value for the PEMA-*r*-AAB copolymer's assembly was calculated to be R_g/R_H =

1.0. It provided evidence of vesicular morphology of PEMA-*r*-AAB copolymer's assembly ($V_{PEMA\text{-}AAB}$) [32,33]. This vesicular morphology was even further supported by microscopy techniques. The effective self-assembly of PEMA-*r*-AAB into quasi-spheric nanoparticles (NPs) of uniform size and the compact membrane was verified in the micrographs obtained by negatively stained transmission electron microscopy (TEM) and bright field scanning transmission electron microscopy (STEM) (Figures 1C and 3F, respectively). The average diameter of $V_{PEMA\text{-}AAB}$ was 87 ± 21 nm (n = 100) by TEM and 95 ± 12 nm (n = 500) by bright field STEM. The polymersome morphology was clearly evidenced in the zoomed-in version of negatively stained TEM and transmission electron cryomicroscopy (Cryo-TEM), as shown in Figures 1D-E. The average bilayer membrane thickness (M_{ave}) of well-defined unilamellar $V_{PEMA\text{-}AAB}$ calculated from TEM micrographs was 10.0 ± 1.8 nm (n = 200, see Figure 3G-H). This result indicates that substituting 53.5 % of the PEMA-*r*-AAB with *p*-AAB is enough for its self-assembly into polymersomes.

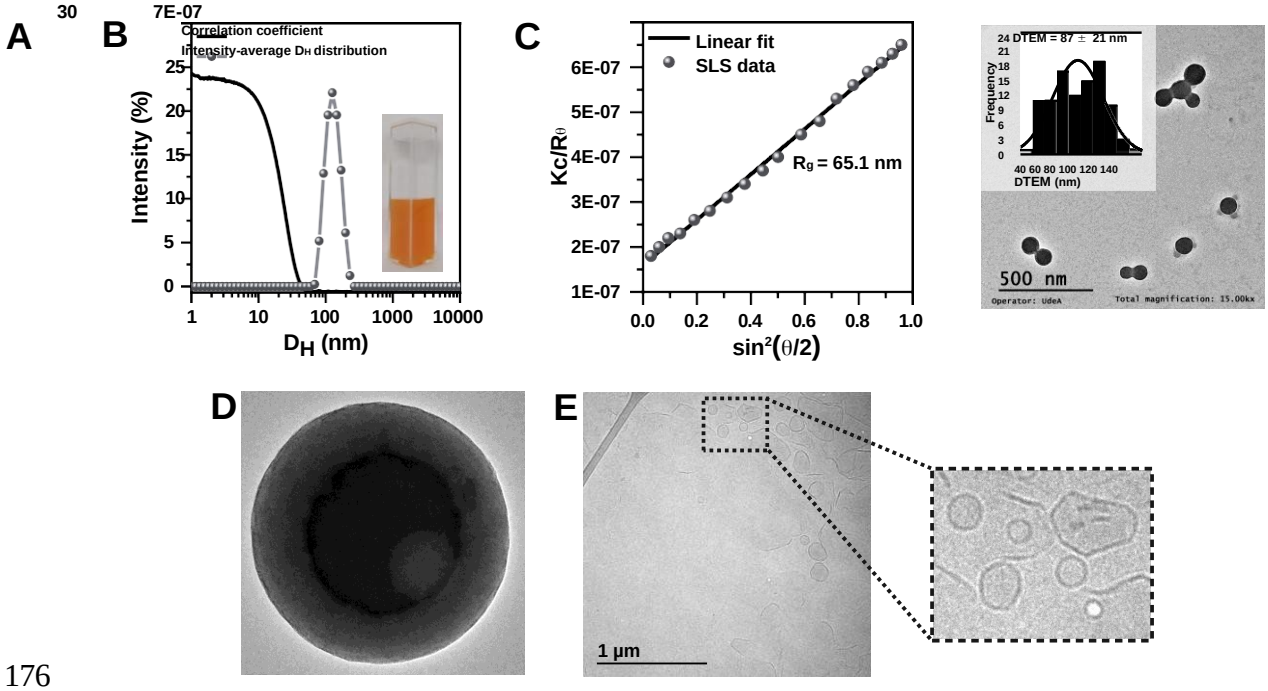

Figure 1. Self-assembly and structure of PEMA-*r*-AAB copolymer. A) Intensity-average D_H distribution, autocorrelation function and solution in cubete real picture, and **B)** Guinier plot of $V_{PEMA\text{-}AAB}$ in H_2O pH 4.0. **C)** Representative negative stained TEM micrograph (scale bar = 500 nm) of $V_{PEMA\text{-}AAB}$ in H_2O pH 4.0 with corresponding size distribution histograms as inset and **D)** zoomed-in negative stained TEM micrograph from C. **E)** Representative Cryo-TEM micrograph (scale bar = 1 µm) and zoomed-in version of $V_{PEMA\text{-}AAB}$ in H_2O pH 4.0.

Electrophoretic light scattering (ELS) study of $V_{PEMA\text{-}AAB}$ proved a negative surface charge with a ζ-potential of -65.68 ± 0.18 mV at pH 4.0, related to the high amount of carboxylic acid groups on the outermost surface of $V_{PEMA\text{-}AAB}$ (Table 1).

Table 1. Summary of hydrodynamic diameter (D_H), dispersity (Đ), and ζ-Potential values for empty and loaded $V_{PEMA\text{-}AAB}$ and $V_{PEMA\text{-}AAB\text{-}biotin}$ as determined by DLS and ELS analysis.

Polymersome	(nm)[a]	Đ[a]	ζ-potential (mV)[b]
$_{PEMA\text{-}AAB}$	125.2 ± 1.3	0.043 ± 0.006	-65.68 ± 0.18
$_{PEMA\text{-}AAB\text{-}biotin}$	100.6 ± 0.7	0.137 ± 0.009	-66.36 ± 1.57
$_{15\%}$-$V_{PEMA\text{-}AAB}$	131.5 ± 0.9	0.062 ± 0.008	-55.37 ± 0.28
$_{25\%}$-$V_{PEMA\text{-}AAB}$	76.5 ± 1.4	0.062 ± 0.008	-60.24 ± 0.28
$MB_{5\%}$-$V_{PEMA\text{-}AAB}$	93.8 ± 0.9	0.224 ± 0.009	-53.78 ± 2.31
$MB_{10\%}$-$V_{PEMA\text{-}AAB}$	141.1 ± 1.2	0.125 ± 0.007	-58.57 ± 0.92
Pt-$V_{PEMA\text{-}AAB}$	108.9 ± 0.7	0.136 ± 0.004	-60.67 ± 1.24
HRP-$V_{PEMA\text{-}AAB}$	132.7 ± 1.6	0.092 ± 0.017	-46.45 ± 0.48
HRP-$V_{PEMA\text{-}AAB\text{-}biotin}$	148.1 ± 2.2	0.232 ± 0.008	-51.06 ± 1.62

[a] D_H and Đ values determined by DLS. [b] ζ-potential values determined by ELS. *All polymersomes were dispersed in H_2O pH 4.0.

After the polymersomes morphology was confirmed, we investigated their structural stability, defined herein as their capacity to maintain the intensity-average hydrodynamic diameter (D_H) distribution and morphology. First, we monitored the temperature-dependent $V_{PEMA\text{-}AAB}$ stability. The structural stability of $V_{PEMA\text{-}AAB}$ in H_2O pH 4.0 was maintained over the temperature range of 25–70 °C as confirmed by temperature-dependent D_H distributions in Figure 2A, exhibiting only a slight increase of about 8 nm at 70 °C, as the temperature does not promote the geometric isomerization from *trans*-to- *cis* AZO moieties.

We assessed the impact of tuning the ion type and concentration on structural stability. According to Figure 2B, $V_{PEMA\text{-}AAB}$ was very stable in aqueous solutions (pH 4.0) containing up to 1.0 M NaCl, KCl, or KNO_3. D_H increased about 700 nm in response to an increase in the external concentrations of NaCl and KCl (2.0 M) throughout a short period (< 5 min). A while later, $V_{PEMA\text{-}AAB}$ disassembled into individual polymeric chains, and no DLS signals were

registered. The D_H was unaffected by KNO_3 at the same concentration. Therefore, rather than cations (i.e., potassium (K^+), and sodium (Na^+)), the loss of structural stability is linked to the high concentration of chloride ions (Cl^-). We could speculate a plausible explanation based on the Hofmeister effect, considering Cl^- competes with carboxylic acid groups on the outermost surface of $V_{PEMA\text{-}AAB}$ to interact with water molecules. Even though the interaction $V_{PEMA\text{-}AAB}$–water is tight because of the charge density per unit area on $V_{PEMA\text{-}AAB}$, the surrounding water molecules' hydrogen bonds (bulk surface) are weakened and broken in excess of Cl^-, causing the remaining water molecules to reorganize [34]. As a result, water molecules rearrange in the hydration layers of the Cl− [35]. The solvation layer of $V_{PEMA\text{-}AAB}$ is consequently less hydrated due to the weaker interaction of the transition water layer with the third water layer (bulk surface). When solvation is lost, non-covalent interactions in the bilayer are insufficient to keep the structure intact, and $V_{PEMA\text{-}AAB}$ quickly disassembles, leading to a salting-out behavior. Instead, nitrate ions (NO_3^-) do not disturb the interaction between the transition and solvation layers of $V_{PEMA\text{-}AAB}$ because of their high volume, intense polarization, and weakly hydrated nature. This anion exhibits a salting-in behavior solubilizing $V_{PEMA\text{-}AAB}$.

Up to this point, the capacity of negative ions to induce structural instability follows the order of the Hofmeister series as $Cl^- > NO_3^-$. According to this series, NO_3^- is classified as a chaotropic anion, while Cl^- is the borderline between kosmotropic/chaotropic anions [34]. Herein, they acted mainly as a kosmotropic anion, so we evaluated the effect of the buffer pH and ionic strength of two kosmotropic anions (citrate and phosphate) on $V_{PEMA\text{-}AAB}$ structural stability (Figure 2C). Even with increased salt concentration, $V_{PEMA\text{-}AAB}$ dispersed in sodium citrate buffer (SC) was as stable at pH 4.0 as in the water. However, at pH 5.5, $V_{PEMA\text{-}AAB}$ swelled to large particles with an average D_H of 220 nm in 0.01 and 0.1 M SC. In 1X phosphate-buffered (PB, 0.01 M phosphate) and 1X phosphate-buffered saline (PBS, 0.137 M NaCl, 0.0027 M KCl, and 0.01 M phosphate), the distribution shifted from monomodal to bimodal, with a population of approximately the same initial size, while others shrank to smaller particles. Independently of the buffer, the bimodal distribution was also seen at pH 7.4. It is notable from Figure 2C that $V_{PEMA\text{-}AAB}$ was sensitive to the medium used to stabilize the pH, with two opposite behaviors, swelling and shrinking.

To explain the swelling process, we considered the $V_{PEMA\text{-}AAB}$ polyacid macrostructures altered by ionization at various pH levels [15,36]. According to the pka values, the carboxylic acid groups on the outermost surface of $V_{PEMA\text{-}AAB}$ gradually dissociate as the dispersion's pH grows. Subsequently, the hydrogen bonds among the groups on the polymersomes' surface decrease, and the negative charge increases, enhancing electrostatic repulsion among the polymeric chains and the hydrophilicity of the outer corona [15,36]. These events led to the $V_{PEMA\text{-}AAB}$ swelling, which was only observed when the pH increased from 4.0 to 5.5 in SC.

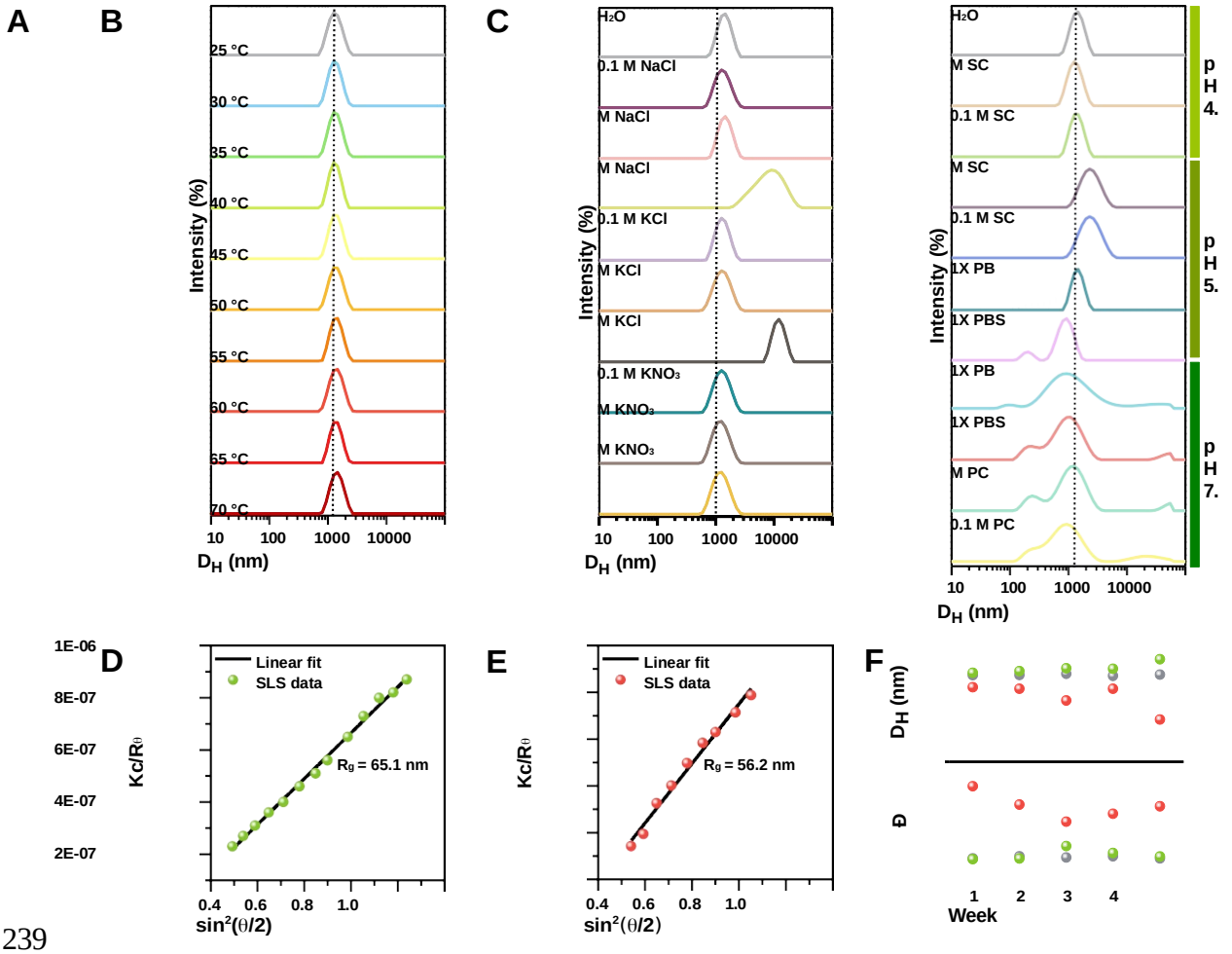

Figure 2. Stability tests of $V_{PEMA\text{-}AAB}$ measured by DLS and SLS. Intensity-average D_H distribution recorded for the aqueous dispersion of $V_{PEMA\text{-}AAB}$ at varying **A)** temperatures, **B)** ionic strength and salt type (pH 4.0), and **C)** combinations of pH, ionic strength, and salt type. *All DLS measurements were taken immediately after preparing samples (Figures A, B, C), except for 1X PB pH 5.5 (Figure 2C short dot intensity-average D_H distribution was measured after 20 min of sample preparation). Guinier plot of $V_{PEMA\text{-}AAB}$ dispersed in **D)** 0.1 M SC pH 4.0 and **E)** 1X PBS pH 7.4. **F)** Evolution in

the time of the D_H and Đ of $V_{PEMA-AAB}$ in H_2O pH 4.0 (●), 0.1 M SC pH 4.0 (●), and 1X PBS pH 7.4 (●).

The effect of the kosmotropic anion must also be considered in the swelling process. When the pH rises, the citrate's degree of ionization varies depending on its pKa values, which may modify the interactions between citrate–water and $V_{PEMA-AAB}$–water, contributing to the $V_{PEMA-AAB}$ structural instability. Be aware that at the same pH where swelling occurred in SC, $V_{PEMA-AAB}$ exhibited the opposite behavior in PB and PBS. When $V_{PEMA-AAB}$ was dispersed in PB as opposed to PBS, it took longer for the size distribution change to reach equilibrium. Thus, despite the low concentration of Cl^-, it may be inferred that the Cl^- and phosphate ions in PBS have a synergistic impact that causes the size distribution to alter more quickly. The driving force of shrinking would be osmotic pressure, caused by the salts incorporated into the $V_{PEMA-AAB}$ dispersion, pushing water out of the cavity and releasing the osmotic energy through deflation [37,38]. The different interactions in the presence of phosphate ions should be a coexisting effecter. As predicted, the Kosmotropic properties of both salts (citrate and phosphate) at different pH values resulted in structural instability of the polymersomes. Based on these findings, we assessed the impact of the dispersing medium on the morphological change of $V_{PEMA-AAB}$ dispersed in 0.1 M SC pH 4.0 and 1X PBS pH 7.4, considering the R_g/R_H ratio. For $V_{PEMA-AAB}$ dispersed in 0.1 M SC pH 4.0, the R_H and R_g were 64.2 nm (Figure 2C) and 65.1 nm (Figure 2D), respectively, resulting in a 1.0 R_g/R_H ratio. It suggests that $V_{PEMA-AAB}$ maintains its vesicular morphology in 0.1 M SC pH 4.0. In contrast, $V_{PEMA-AAB}$ dispersed in 1X PBS pH 7.4 exhibited a bimodal size distribution (Figure 2C) with R_H values of 11.1 nm for the first size population and 55.0 nm for the second one. As the R_g value was 56.2 nm (Figure 2E), the R_g/R_H ratio was >> 1.0 for the first size population and 1.0 for the second one, indicating that the morphology of $V_{PEMA-AAB}$ is only partially retained when dispersed in 1X PBS pH 7.4.

Therefore, we linked the loss of structural stability with (i) changes in the intensity-average size distribution, observed as the swelling, shrinking, or disassembling of $V_{PEMA-AAB,}$ and (ii) morphological changes. In agreement, many authors have reported salt- and pH-dependent changes in the size distribution and shape of the polymersomes [37–40], e.g., ellipsoids, tubes, discs, stomatocytes, and large compound vesicles. It is attributed to osmotic pressure;

water–water, ion–water, polymersomes' membrane–water and polymersomes' membrane–ion interactions; and fusion processes, depending on the specific ion type [37,38].

Finally, we monitored the D_H and dispersity (Đ) of $V_{PEMA\text{-}AAB}$ over time for up to four weeks in H_2O pH 4.0, 0.1 M SC pH 4.0, and 1X PBS pH 7.4, as shown in Figure 2F. $V_{PEMA\text{-}AAB}$ was highly stable in water, keeping their size and low dispersity even for one month. However, during the four weeks of storage, $V_{PEMA\text{-}AAB}$ slightly increased in size in 0.1 M SC pH 4.0, about 17 nm. In contrast, $V_{PEMA\text{-}AAB}$ in 1X PBS pH 7.4 presented a substantial variability in size, as was explained before. Additional experiments in these media are shown below.

The counterpart $V_{PEMA\text{-}AAB\text{-}biotin}$ was smaller and more dispersed than $V_{PEMA\text{-}AAB}$ due to the size of the biotin molecule relative to the other side groups while retaining the electrostatic stability (Figure S4A and Table 1). A homemade colorimetric magneto-assay corroborated the presence of biotin moieties on the outermost surface of $V_{PEMA\text{-}AAB\text{-}biotin}$. The polyHRP20–$V_{PEMA\text{-}AAB\text{-}biotin}$–MB magnetoconjugates were produced and catalyzed the oxidation of non-colored 3,3,5,5'-Tetramethylbenzidine (TMB, diamine) to one-electron oxidation product (cation-radical compound, $TMB_{OXD\text{-}1e}$) and two-electrons oxidation product (diimine, $TMB_{OXD\text{-}2e}$) in the presence of hydrogen peroxide (H_2O_2). The unoxidized TMB forms a blue charge-transfer complex with the two-electron oxidation product (diamine/diamine, TMB/$TMB_{OXD\text{-}2e}$) with maximum absorbance at 652 nm (Figure S4B) [41]. According to the UV-vis absorption spectra, polyHRP20–$V_{PEMA\text{-}AAB\text{-}biotin}$–MB conjugation was less effective in H_2O pH 4.0 than in 0.1 M SC pH 4.0 and 1X PBS pH 7.4. Interestingly, $V_{PEMA\text{-}AAB}$, laking biotin, did not change color (inset photographs in Figure S4B), confirming that the biotin-free polymersomes do not possess any binding affinity toward streptavidin. Furthermore, $V_{PEMA\text{-}AAB\text{-}biotin}$ retained the same structural stability as $V_{PEMA\text{-}AAB}$ upon time in H_2O pH 4.0, 0.1 M SC pH 4.0, and 1X PBS pH 7.4, toward temperature, and in the presence of salts (NaCl, KCl, KNO_3), as shown in Figures S4C-E. In the different kosmotropic media, $V_{PEMA\text{-}AAB\text{-}biotin}$ was stable at pH 4.0, while simultaneous swelling and shrinking were observed at pH ≥ 5.5, as seen in Figure S4F. This behavior might be explained in the same fashion as per $V_{PEMA\text{-}AAB}$, considering the presence of biotin moieties on the outermost surface of $V_{PEMA\text{-}AAB\text{-}biotin}$.

3.3. UV-induced $V_{PEMA\text{-}AAB}$ and $V_{PEMA\text{-}AAB\text{-}biotin}$ transition

We investigated the UV-induced evolution of $V_{PEMA\text{-}AAB}$ and $V_{PEMA\text{-}AAB\text{-}biotin}$ in aqueous media. Figures 3A-C and S5A-C show the UV irradiation time-dependent UV-vis absorption spectra of $V_{PEMA\text{-}AAB}$ and $V_{PEMA\text{-}AAB\text{-}biotin}$ dispersed in H_2O pH 4.0, 0.1 M SC pH 4.0, and 1X PBS pH 7.4.

The UV irradiation causes a gradual decrease of the π-π* transition band at 341 nm and a slight increase of the n-π* transition band at ca. 450 nm owing to photochemical *trans*-to-*cis* isomerization of AZO moieties [12–14]. This geometric transition is accompanied by a color change in $V_{PEMA\text{-}AAB}$ dispersion, from orange to yellow tinge in H_2O pH 4.0 and 0.1 M SC pH 4.0 (inset photographs in Figures 3A-B). The photoinduced isomerization in H_2O pH 4.0 and 1X PBS pH 7.4 occurred quickly within ∼60 s of UV irradiation, reaching a photostationary state, while it was reached after 300 s in 0.1 M SC pH 4.0 (Figures 3D and S5D). The isomerization degree extent at 600 s was ca. of 37.0, 41.0, and 62.0 % for both $V_{PEMA\text{-}AAB}$ and $V_{PEMA\text{-}\ AAB\text{-}biotin}$ in H_2O pH 4.0, 0.1 M SC pH 4.0, and 1X PBS pH 7.4, respectively. UV irradiation time-dependent DLS measurements were conducted to monitor the evolution of intensity-average D_H and Đ (Figure 3E and S5E). The intensity-average D_H and Đ remained almost unchanged upon UV irradiation for $V_{PEMA\text{-}AAB}$ and $V_{PEMA\text{-}AAB\text{-}biotin}$ in H_2O pH 4.0. Polymersomes dispersed in H_2O pH 4.0 remained stable after UV irradiation mainly by hydrophobic interactions in the polymersomes' membrane. The increase in the isomerization degree in 0.1 M SC pH 4.0 and 1X PBS pH 7.4 concerning H_2O pH 4.0 increased D_H. In 0.1 M SC pH 4.0, it increased from 128.3 ± 1.1 to 143.1 ± 3.0 nm and from 110.9 ± 0.9 to 126.8 ± 0.9 (n = 6) nm for $V_{PEMA\text{-}AAB}$ and $V_{PEMA\text{-}AAB\text{-}biotin}$, respectively, with a constant Đ value. In contrast, D_H in 1X PBS pH 7.4 significantly increased.

Please note that the longer time required to reach the photostationary state through photoinduced isomerization of $V_{PEMA\text{-}AAB}$ in 0.1 M SC pH 4.0, compared to H_2O pH 4.0, could be attributed to specific electrostatic interactions between SC and the carboxylic acid groups on the outermost surface of $V_{PEMA\text{-}AAB}$. These interactions limit the degrees of freedom of the azo-based polymeric chains, thereby slowing down the rate of *cis*-to-*trans* interfacial interconversion. Notably, the effect is entirely the opposite in 1 X PBS pH 4.0, where there is a clear correlation among the loss of structural stability described in the previous section, the time to reach the photostationary state and the degree of isomerization. We speculate that the spatial reorganization of the AZO moieties due to the shrinking of $V_{PEMA\text{-}AAB}$ in 1X PBS pH

7.4 results in a higher degree of freedom of AZO moieties, promoting their maximum isomerization degree in a short time, as reported [13].

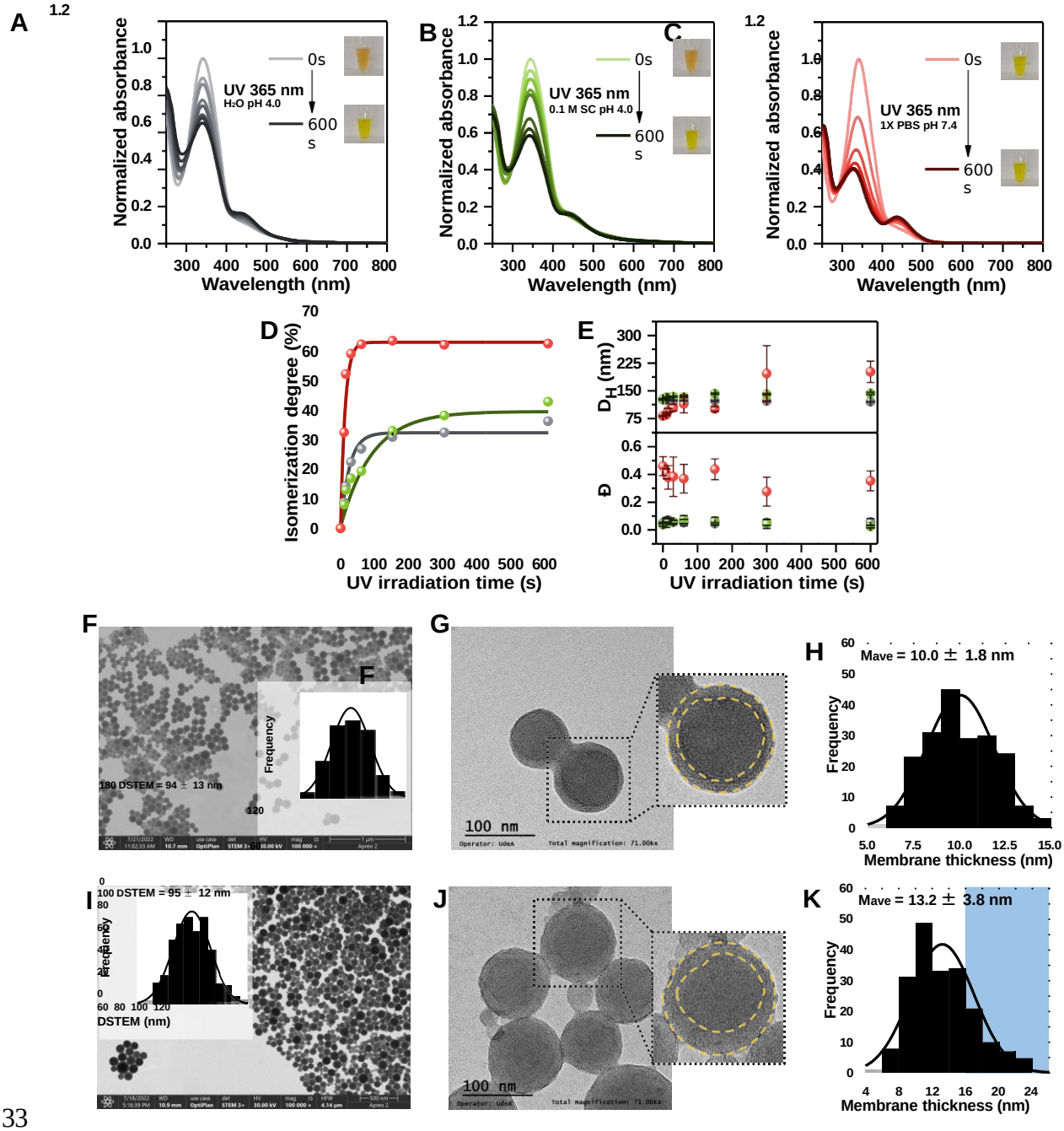

Figure 3. $V_{PEMA-AAB}$ transition upon UV irradiation characterized by UV-vis, DLS and TEM.

Evolution of $V_{PEMA-AAB}$ UV-vis absorption spectra induced by photoisomerization in **A)** H_2O pH 4.0, **B)** 0.1 M SC pH 4.0, and **C)** 1X PBS pH 7.4 upon time. The UV-vis absorption spectra were normalized with $t_{irradiation}$ = 0 s. **D)** Isomerization degree upon irradiation time in H_2O pH 4.0 (—●—), 0.1 M

SC pH 4.0 (), and 1X PBS pH 7.4 (). **E)** Evolution of the intensity-average D_H and Đ of $V_{PEMA\text{-}AAB}$ after irradiation in H_2O pH 4.0 (), 0.1 M SC pH 4.0 (), and 1X PBS pH 7.4 (). Repre-

sentative negative stained bright field STEM micrographs of $V_{PEMA\text{-}AAB}$ in H_2O pH 4.0 with the corresponding size distribution histograms in the inset **F)** before ($t_{irradiation}$ = 0 s, scale bar = 1000 nm), and **I)** after irradiation ($t_{irradiation}$ = 600 s, scale bar = 500 nm). Representative negative stained TEM micrographs and zoomed-in version of $V_{PEMA\text{-}AAB}$ in H_2O pH 4.0 **G)** before ($t_{irradiation}$ = 0 s, scale bar = 100 nm), and **J)** after irradiation ($t_{irradiation}$ = 600 s, scale bar = 100 nm). Histograms of membrane thickness distribution along with calculated average membrane thickness values **H)** before ($t_{irradiation}$ = 0 s), and **K)** after irradiation ($t_{irradiation}$ = 600 s).

STEM micrographs of $V_{PEMA\text{-}AAB}$ in H_2O pH 4.0 before and after 600 s UV irradiation revealed preservation of size (Figures 3F and 3I) according to DLS results, while negatively stained TEM micrographs confirmed that the morphology was preserved (Figures 3G and 3J). Nevertheless, the photoinduced isomerization of AZO moieties at the interface caused a change in the hydrophobic packing, thereby compromising the integrity of the bilayer membrane through its irregular deformation and fluctuations in thickness. The calculated M_{ave} increased from 10.0 ± 1.8 nm to 13.2 ± 3.8 nm (n = 200) after 600 s UV irradiation (Figures 3H and 3K). Although the M_{ave} values are close, the population larger than 16 nm evidenced increased membrane thickness (Figure 3K). The morphology of $V_{PEMA\text{-}AAB}$ dispersed in 1X PBS pH 7.4 was unclear in the negatively stained TEM micrographs (Figure S6A-B) because uranyl acetate precipitates noticeably when the pH is over pH 5.0 [42].

3.4. Hydrophobic and hydrophilic cargo encapsulation within $V_{PEMA\text{-}AAB}$

We demonstrated that the $V_{PEMA\text{-}AAB}$ serves as a reservoir for hydrophobic and hydrophilic cargoes of different chemical natures within the corresponding compartments. The bilayer membrane served as a reservoir of hydrophobic molecules, as demonstrated by incorporating water-insoluble ferrocene (Fc). Hydrophilic molecules like methylene blue (MB), inorganic platinum NPs stabilized with SC (Pt@SC NPs), and enzymes like horseradish peroxidase (HRP) might all fit inside the aqueous core of these vesicular assemblies. Figure S7 shows the changes in intensity-average D_H distribution and autocorrelation function for each polymersome dispersion. The values of D_H and Đ are reported in Table 1. Fc-, MB-, Pt-, and HRP-loaded $V_{PEMA\text{-}AAB}$ had minor variations in size. Figure S7 also shows the cargo-dependent physical changes as inset photographs. The color changes of each dispersion indicate the successful encapsulation depending on the kind of cargo and the amount attempted to encapsulate. The color and intensity-average D_H distribution of the Fc- MB-, and HRP-loaded $V_{PEMA\text{-}AAB}$ did not change over time, suggesting high encapsulation stability and cargo retention. Pt-$V_{PEMA\text{-}AAB}$ precipitated after two months. ζ-potential values for loaded polymersomes

were like $V_{PEMA-AAB}$, except for HRP-$V_{PEMA-AAB}$, due to the adsorption of HRP on the polymersomes' surface (Table 1). Encapsulation efficiency, loading capacity, and cargo concentration values are reported in Table S3. As expected, the encapsulation of hydrophobic compounds was low due to the bilayer membrane's low thickness and high compactness. On the contrary, hydrophilic molecules were highly efficiently encapsulated, associated with the higher volume of the aqueous core and the electrostatic interactions between MB and groups on the innermost surface of $V_{PEMA-AAB}$. The encapsulation efficiency for HRP-$V_{PEMA-AAB}$ turned out to be higher than in other works [43–45], related to the adsorption of HRP on the polymersomes' surface, according to the reported ζ-potential value.

Figure 4A shows the overlap between the number-average D_H distributions for Pt@SC NPs and Pt-$V_{PEMA-AAB}$. Be aware that no signal was associated with the Pt@SC NPs in the number-average D_H distributions of the Pt-$V_{PEMA-AAB}$, demonstrating that Pt@SC NPs were encapsulated inside $V_{PEMA-AAB}$. The significant light scattering of Pt@SC NPs forced us to compare the size distribution by number. The encapsulation and distribution of Pt@SC NPs in the polymersomes' aqueous core are depicted in the negatively stained TEM micrograph of Figure 4B. The interplanar spacing for Pt of the 111 planes is displayed by zooming in on the Pt-$V_{PEMA-AAB}$ aqueous core in Figure 4C [46]. Although negatively charged cargoes would be hardly encapsulated, Pt@SC were indeed successfully encapsulated. This is presumably because the $V_{PEMA-AAB}$ was stable in the presence of SC at low pH, as we had previously shown. The gradual instability, however, might be brought on by the electrostatic repulsion between the citrate-capped PtNPs and the innermost surface of Pt-$V_{PEMA-AAB}$.

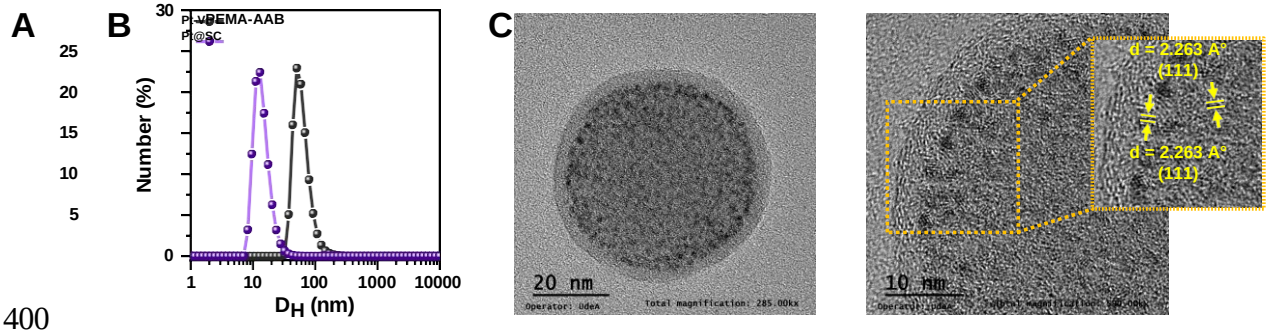

Figure 4. Pt-$V_{PEMA-AAB}$ characterization by DLS and TEM. A) Number-average D_H distribution of Pt-$V_{PEMA-AAB}$ and Pt@SC NPs in H_2O pH 4.0. Representative negative stained TEM micrograph of Pt-$V_{PEMA-AAB}$ in H_2O pH 4.0 in **B)** complete version (scale bar = 20 nm), and **C)** zoomed-in version (scale bar = 10 nm).

3.5. UV-induced release of MB from $MB_{10\%}$-$V_{PEMA\text{-}AAB}$

One possible application for the polymersomes designed here is the on-demand cargo release. To investigate the UV-induced release of small water-soluble molecules, we employed the $MB_{10\%}$-$V_{PEMA\text{-}AAB}$ to measure the release of MB. The cargo release from AZO-based polymersomes could only occur when the AZO moieties are isomerized [47,48]. In this context, rather than spectrophotometry, fluorescence, or HPLC commonly used to characterize cargo release, we developed a rapid, simple, and sensitive electrochemical assay to monitor the UV-induced release of MB from $MB_{10\%}$-$V_{PEMA\text{-}AAB}$ in real-time. This approach differs from other methods that monitor cargo release via electrochemical techniques [19–23]. We used cyclic voltammetry (CV) at disposable screen-printed carbon electrodes (SPCEs) in 0.1 M SC pH 4.0 and 1X PBS pH 7.4 (Scheme S3). Figures 5A-B show representative cyclic voltammograms for the MB release in 0.1 M SC pH 4.0 and 1X PBS pH 7.4, respectively. The continuous stimulation of $MB_{10\%}$-$V_{PEMA\text{-}AAB}$ with UV light at 365 nm led to a rapid increase in cathodic and anodic currents associated with MB oxidoreduction, indicating that the polymersomes' membrane became permeable for MB. Interestingly, with increasing pH, the cathodic and anodic peak potentials (Ec, and Ea, respectively) shifted negatively at the same scan rate. In 0.1 M SC pH 4.0, Ec and Ea values were -0.14 V and -0.10 V, while in 1X PBS pH 7.4, they were -0.32 V and -0.25 V. Moreover, the peak current increased with increasing pH. All these changes can be explained through the pH-depend MB oxidoreduction mechanism, described as an electron-transfer process with an intervening proton-transfer process (ECE) [49]. The redox reaction at pH < 5.4 is a two-electron-three-proton-transfer process, while that at pH > 6.0 is a two-electron-one-proton-transfer process [49]. Despite this, cyclic voltammograms in Figures 5A-B show that the reaction intermediate is hardly ever present. As a result, the shape of the cyclic voltammetric curves is almost pH-independent, except for the slight shift of the cathodic and anodic peaks and the current values with pH.

Figures 5C-D reveal that, after just 432 s of continuous irradiation, $MB_{10\%}$-$V_{PEMA\text{-}AAB}$ had cumulative release extents of 59.8 % in 0.1 M SC pH 4.0 and 95.6 % in 1X PBS pH 7.4. No such release of MB was observed in the dark from $MB_{10\%}$-$V_{PEMA\text{-}AAB}$ dispersed in 0.1 M SC pH 4.0. In this case, the physisorbed MB on the outermost surface of $MB_{10\%}$-$V_{PEMA\text{-}AAB}$ underwent oxidoreduction, resulting in a minimal increase in the current of the cathodic and anodic peaks (Figure S9A). In contrast, when $MB_{10\%}$-$V_{PEMA\text{-}AAB}$ were dispersed in 1X PBS

pH 7.4, the current remarkably increased (Figure S9D), and the release extent increased from 10.2 to 49.2 % without irradiation conditions. $MB_{10\%}$-$V_{PEMA\text{-}AAB}$ were also exposed to alternating cycles of UV irradiation and darkness (non-continuous irradiation). As reported, the current grew throughout the irradiation cycles but slowed down without light [47]. In this scenario, we suggest that the bilayer membrane acts as a barrier to maintain the proper balance of MB inside and outside $MB_{10\%}$-$V_{PEMA\text{-}AAB}$ during darkness cycles. Compared to conventional AZO and pseudo-stilbene, the *cis* isomer of AZO with one electron-donating group has an intermediate lifetime [13]. Therefore, if reconversion to the *trans* from *cis* isomer is not promoted, $MB_{10\%}$-$V_{PEMA\text{-}AAB}$ remains permeable even in the dark. Furthermore, as the cycles of UV irradiation increased (192 s of UV irradiation), the systems reached their corresponding photostationary states (Figure 3D). Under these conditions, the cumulative release extents of MB from $MB_{10\%}$-$V_{PEMA\text{-}AAB}$ were 23.5 and 82.6 % in 0.1 M SC pH 4.0 and 1X PBS pH 7.4, respectively.

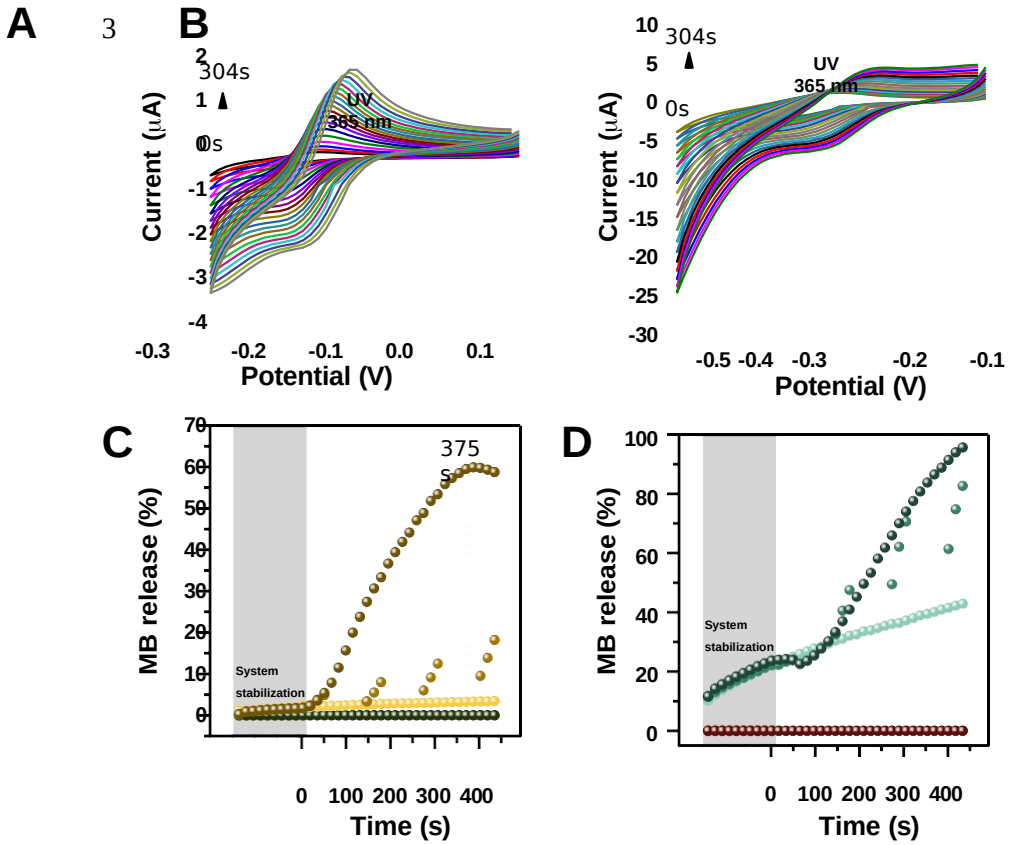

Figure 5. UV-induced release of MB from $MB_{10\%}$-$V_{PEMA\text{-}AAB}$. Cyclic voltammograms of $MB_{10\%}$-$V_{PEMA\text{-}AAB}$ under continuous UV irradiation in **A)** 0.1 M SC pH 4.0 and **B)** 1X PBS pH 7.4. All cyclic voltammograms contain 19 representative cycles corresponding to 304 s of measurements. **C)** MB

release extent from $MB_{10\%}$-$V_{PEMA\text{-}AAB}$ in 0.1 M SC pH 4.0 with continuous UV irradiation (●), alternating UV and darkness cycles (●), and in darkness (●). $V_{PEMA\text{-}AAB}$ during continuous UV irradiation (●), and in darkness (●) is also shown as a negative control. **D)** MB release extent from $MB_{10\%}$-$V_{PEMA\text{-}AAB}$ in 1X PBS pH 7.4 with continuous UV irradiation (●), alternating UV and darkness cycles (●), and in darkness (●). $V_{PEMA\text{-}AAB}$ during continuous UV irradiation (●), and in darkness (●) is also shown as a negative control.

Continuous stimulation resulted in 2.5-fold and 1.1-fold more MB release in 0.1 M SC pH 4.0 and 1X PBS pH 7.4, respectively, than non-continuous stimulation. $V_{PEMA\text{-}AAB}$ was subjected to continuous UV stimulation or darkness procedures as a control. In none of the procedures, oxidoreduction peaks were observed in the potential windows for $V_{PEMA\text{-}AAB}$ dispersed in 0.1 SC pH 4.0 (Figures S9B-C) or 1X PBS pH 7.4 (Figures S9E-F), suggesting that engineered polymersomes were not electroresponsive. Therefore, photostimulation might be responsible for the MB release. During photostimulation, the conformational switch between the *trans* and *cis* isomers is accompanied by the reorientation of AZO moieties and the increase of the molecular dipole moment [12–14]. These processes make the hydrophobic bilayer membrane slightly more hydrophilic and, as a result, permeable for water-soluble molecules.

The molecular rearrangement and polarity change in the bilayer membrane explain the MB release in 0.1 SC pH 4.0 but not enough in 1X PBS pH 7.4. As the pH increased, the relative magnitude of release extent with and without photostimulation was higher. Our earlier findings demonstrated that $V_{PEMA\text{-}AAB}$ was pH-sensitive as well. As a result, the MB release is significantly influenced by the nature and composition of the surrounding solution, plus the photostimulation. The changes in size distribution, morphology, and the isomerization degree explained previously could cause the difference in MB release in the two media. When the polymersomes were dispersed in 1X PBS pH 7.4, their size distribution changed, which appeared to cause a quick and continuous MB release. However, whether or not photostimulation is constant, it is evident that the release was favored because of the high degree of isomerization in a short time and the associated size shift (Figures 3D-E).

According to these results, $V_{PEMA\text{-}AAB}$ presented two medium-dependent release profiles: (i) intermittent photorelease, with cargo release halting in the dark and resuming when exposed to light, in acidic conditions (0.1 M SC, pH 4.0), and ii) continuous cargo release in a more

alkaline medium such as 1X PBS pH 7.4, significantly enhanced by irradiation. This characteristic can be advantageous for applications requiring rapid cargo release, such as biosensors. The medium-mediated release mechanism offers an advantageous approach, allowing for controlled and timely release, critical for biosensor performance. In this context, the noticeable improvement in the MB release profile in 1X PBS pH 7.4, even in dark conditions due to the reorganization of the polymersomes, could be beneficial for electrochemical biosensing applications. These conditions ensure optimal release, which is essential for achieving the highest analytical signal of MB [50,51]. Therefore, MB can be adapted to enhance signal-generating events in label-based electrochemical biosensors [52].

3.6. HRP-$V_{PEMA\text{-}AAB\text{-}biotin}$-labeled sandwich-type immunoassay

Scheme S4 shows the principle of the proposed optical immunosensor based on $V_{PEMA\text{-}AAB\text{-}biotin}$ as a carrier of enzymatic labels (HRP) (physicochemical characterization of HRP-$V_{PEMA\text{-}AAB\text{-}biotin}$ is summarized in Tables 1 and S3). Unlike the conventional enzyme-linked immunosorbent assay (ELISA), in which biotinylated detection antibodies (b-DAb) is labeled with only limited Strep-HRP, more HRP could be integrated into the immunoassay when HRP-$V_{PEMA\text{-}AAB\text{-}biotin}$ was attached to b-DAb because a large amount of HRP was encapsulated in single $V_{PEMA\text{-}AAB\text{-}biotin}$.

The biorecognition events were monitored by optical readout using the TMB/H_2O_2/HRP redox system. The intensity-average D_H distributions shown in Figure S11 indicate that structural stability of $V_{PEMA\text{-}AAB\text{-}biotin}$ was lost in TMB/H_2O_2 substrate solution, with D_H increasing up ca. of 1050 nm after 5 min. A while later, $V_{PEMA\text{-}AAB\text{-}biotin}$ was disassembled into individual polymeric chains, and no DLS signals were registered. As the structural stability was preserved in each of the individual substrates, i.e., TMB and H_2O_2, their structural instability in the presence of TMB/H_2O_2 substrate solution could be attributed to any of their components [53,54]. As a result, the TMB/H_2O_2 substrate solution substrate caused the direct disassembly of the HRP-$V_{PEMA\text{-}AAB\text{-}biotin}$ to release a large amount of HRP, which catalyzed the H_2O_2-mediated TMB oxidation, producing a color change in the system. In this case, HRP-$V_{PEMA\text{-}AAB\text{-}biotin}$ works as a medium-responsive electroactive label release system. The optical detection of IL-6 was monitored by the color change in the system from colorless to blue at a maximum absorbance of 652 nm after 20 min.

Univariate analysis was used to analyze the critical experimental variables influencing the analytical performance of the immunoassay. The evaluated variables were researched within predetermined ranges while other ones remained constant. The absorbance obtained in the presence of 200 pg mL^{-1} (signal, S) and absence (blank, B) of IL-6 standard protein was compared for each value in the tested range.

The starting protocol for the optimizations involved four biomodification steps with solutions containing (i) 50 µg mL^{-1} capture antibody (CAb), (ii) 0 and 200 pg mL^{-1} IL-6 standard protein, (iii) 0.20 µg mL-1 b-DAb, and (iv) 1/100 diluted Strep-HRP-$V_{PEMA\text{-}AAB\text{-}biotin10}$ conjugates. Figure 6 depicts the dependence of the absorbance values measured in the presence of 200 pg $mL^{-1,}$ the absence of IL-6 standard protein, and the resulting S/B ratio for detecting IL-6 when each evaluated variable was modified independently. Table S5 summarizes the evaluated variables, tested ranges, and selected values.

The most influential experimental variables were related to the biotin-Strep-biotin noncovalent binding in the labeled step to achieve better sensitivity. Therefore, the first optimized experimental variable was the PEMA-*r*-AAB-*r*-biotin/Strep ratio (w/w) used in the preincubation step (biofuntionalization of HRP-$V_{PEMA\text{-}AAB\text{-}biotin}$ with Strep). Figure 6A reveals that S/B ratio initially increased as the PEMA-*r*-AAB-*r*-biotin/Strep ratio (w/w) increased from 2.50 to 31.25 and then declined beyond 31.25 when Strep-HRP-$V_{PEMA\text{-}AAA\text{-}biotin}$ conjugates were diluted 1/100. This behavior is directly related to the biotin/Strep ratio. The biotin/Strep is frequently kept constant at a 1:1 ratio (i.e., 4 mol of binding sites) to avoid crosslinking via Strep bridges through biotin-Strep-biotin noncovalent binding [55]. As the amount of biotin on the outermost surface of HRP-$V_{PEMA\text{-}AAA\text{-}biotin}$ is unknown, three scenarios could be considered depending on the PEMA-*r*-AAB-*r*-biotin/Strep ratio. In the first scenario, a low PEMA-*r*-AAB-*r*-biotin/Strep ratio (i.e., 2.50 mg PEMA-*r*-AAB-*r*-biotin/mg Strep) indicates a higher amount of Strep in comparison to biotin, meaning that most of the Strep covers the HRP-$V_{PEMA\text{-}AAA\text{-}biotin}$ while possibly another amount remains unbound. When in contact with the b-DAb/IL-6/CAb/well, unbound Strep may have a much higher binding affinity for b-DAb than Strep-HRP-$V_{PEMA\text{-}AAA\text{-}biotin}$, limiting b-DAb labeling with Strep-HRP-$V_{PEMA\text{-}AAA\text{-}biotin}$ and therefore the signal. The second scenario considers the opposite situation, i.e., the highest PEMA-*r*-AAB-*r*-biotin/Strep ratio (62.50 mg PEMA-*r*-AAB-*r*-biotin/mg Strep). A very high ratio reduces the amount of Strep relative to biotin, promoting biotin-Strep-biotin

noncovalent binding and, therefore, the formation of macroconjugates among HRP-$V_{PEMA-AAA-biotin}$. Due to steric hindrance, these macroconjugates further limit the interaction with the immobilized b-DAb. In the final scenario, the suitable PEMA-*r*-AAB-*r*-biotin/Strep ratio (i.e., 31.25 mg PEMA-*r*-AAB-*r*-biotin/mg Strep) is achieved, in which crosslinking between HRP-$V_{PEMA-AAA-biotin}$ is minimized while binding to b-DAb is favored.

¡Error! No se encuentra el origen de la referencia. 6B shows the optimal Strep-HRP-$V_{PEMA-AAB-biotin}$ dilution factor was 1/100 after preincubation at 31.25 mg PEMA-*r*-AAB-*r*-biotin/mg Strep. The S/B ratio increased significantly with the Strep-HRP-$V_{PEMA-AAA-biotin}$ dilution factor over the range 1/1000 – 1/100. Although the specific signal in the presence of IL-6 standard protein was notably larger to a lower dilution factor than 1/100 (i.e., a higher amount of Strep-HRP-$V_{PEMA-AAA-biotin}$ conjugates), it was also for the blank due to nonspecific adsorption, with which the S/B ratio decreased.

Next, the best medium for b-DAb labeling with Strep-HRP-$V_{PEMA-AAA-biotin}$ conjugates was evaluated. According to the previous stability studies, H_2O pH 4.0, 0.1 M SC pH 4.0, and 1X PBS pH 7.4 in the presence and absence of 1 % (w/v) BSA (i.e., H_2O, SC, SC-BSA, PBS, and PBS-BSA) were tested as media for b-DAb labeling studies. Figure 6C shows that in media containing BSA (i.e., in SC-BSA and PBS-BSA media), the labeling interaction (i.e., biotin-Strep-biotin noncovalent binding) was suppressed. Although Figure 6C only displays this behavior in media containing 1 % (w/v) BSA as a typical concentration in ELISA, lower BSA concentrations also limited labeling interaction (results not shown). Different behaviors were observed in media without BSA. For example, while in H_2O pH 4.0, the labeling interaction was promoted, in 0.1 M SC pH 4.0 and 1X PBS pH 7.4, nonspecific adsorption was observed, possibly due to electrostatic interactions in these media. Therefore, water was selected as the medium for b-DAb labeling with Strep-HRP-$V_{PEMA-AAA-biotin}$ conjugates.

CAb concentration was the following experimental variable optimized (6D). In the presence of CAb, the S/B ratio increased with the CAb concentration from 2.5 – 5 μg mL^{-1} due to the increase in the specific signal in the presence of IL-6 standard protein, with 5 μg mL^{-1} as the optimal. At this concentration, the CAb density on the surface of ELISA wells is appropriate to favor the antibody-antigen recognition event probability because the CAbs' antigen-binding sites (paratopes) are not sterically hindered. When the CAb concentration increased, two situations arose. The first is related to the limitation in the antibody-antigen recognition event

because of a steric hindrance at the antigen-binding sites, and therefore, the specific signal in the presence of IL-6 standard protein decreased. In the second one, their nonspecific absorptions are favored upon CAb concentration, increasing the blank's signal response. Therefore, with a CAb concentration higher than 5 µg mL^{-1} the S/B ratio decreased. It is also noteworthy that in the absence of CAb the signal response in the presence and absence of IL-6 is equal, thus confirming that under optimal conditions, b-DAb labeling with Strep-HRP-$V_{PEMA\text{-}AAA\text{-}biotin}$ conjugates is favored but not the nonspecific absorptions.

In the subsequent optimization, four assembly protocols were tested with sequential biomodification steps of 60 min each, starting from the blocked CAb/well (refer to the materials and methods of SI, section 1.3.9). From the results displayed in Figure 6E, the S/B ratio was notably larger when using protocol I. The stepwise protocol could favor each interaction in a complex assay like the one used in this work, in which nonspecific adsorption competes with b-DAb labeling with Strep-HRP-$V_{PEMA\text{-}AAA\text{-}biotin}$ conjugates. In this way, in the first biomodification step, IL-6/CAb interaction was promoted, while different IL-6 epitopes remained available to interact with b-DAb paratopes in the second biomodification step. The final biomodification with Strep-HRP-$V_{PEMA\text{-}AAA\text{-}biotin}$ conjugates maximized the b-DAb labeling compared to the other protocols. Protocols II, III, and IV potentially limited the antibody-antigen recognition events and b-DAb labeling due to aggregation processes or steric hindrance when the corresponding bioreagents coexisted in the solution, as judged by decreased specific signals in the presence of IL-6 standard protein. In similar assays using biotinylated HRP-loaded vesicles (liposomes), biomodifications with Strep and biotinylated HRP-loaded liposomes were performed independently [53,54,56]. However, this protocol did not discriminate between absorbance values using the HRP-$V_{PEMA\text{-}AAA\text{-}biotin}$ (results not shown).

Finally, the optimal b-DAb concentration was set at 0.20 µg mL^{-1} (Figure 6F), and a longer b-DAb concentration did not enhance the sensitivity. As the CAb and b-DAb concentrations and the general assembly protocol were the same as those reported by the human IL-6 DuoSet ELISA supplier, the incubation times were not optimized. Overall, the results show that the optimal detection of IL-6 using HRP-$V_{PEMA\text{-}AAA\text{-}biotin}$ could be achieved in 170 min only in a protocol involving three biomodification steps. Noteworthy b-DAb labeling can only be

achieved after biofunctionalization of HRP-$V_{PEMA\text{-}AAB\text{-}biotin}$ with Strep, in which the biotin/Strep ratio is the crucial step to avoiding the presence of unbonded Strep or HRP-$V_{PEMA\text{-}AAB\text{-}biotin}$ crosslinking via Strep bridges.

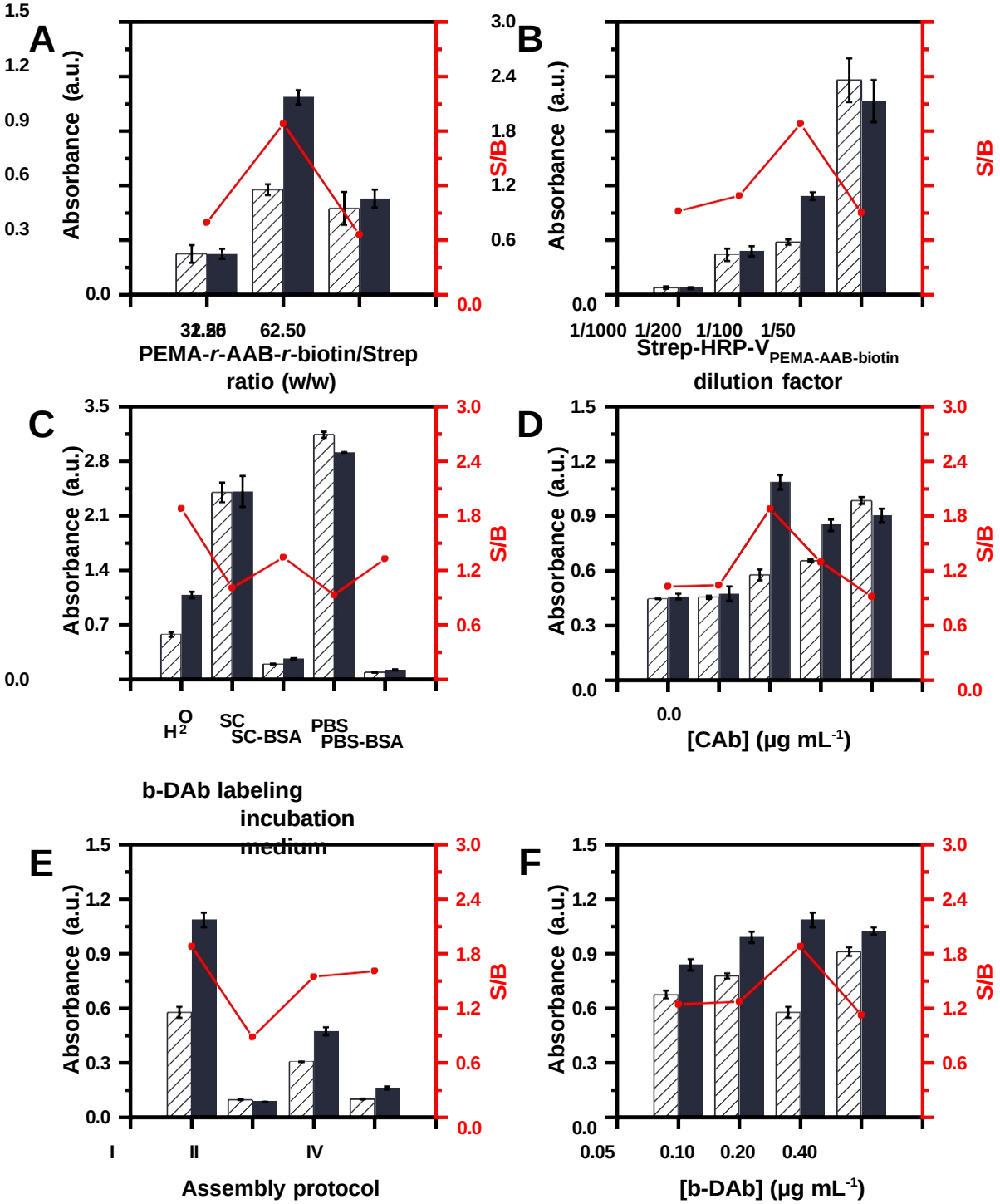

Figure 6. Optimization of critical experimental variables involved in the optical detection of IL-6. Dependence of the optical response measured in the presence of 200 pg mL^{-1} (grey bars) and absence (white pattern bars) of IL-6 standard protein and the resulting signal-to-blank ratio (S/B, red

613 lines) with **A)** PEMA-*r*-AAB-*r*-biotin$_{10}$/Strep ratio; **B)** Strep-HRP-V$_{\text{PEMA-AAB-biotin10}}$ dilution factor;

C) b-DAb labeling incubation medium; **D)** CAb concentration; **E)** assembly protocol involving sequential biomodifications in (I) three steps, (II-III) two steps, and (IV) one step, (see main text); **F)** b-DAb concentration. Error bars were estimated as the measurement's standard deviation (n = 2).

4. CONCLUSIONS

The work covered four key aspects: (i) the synthesis of a new class of multicoordinated and multifunctional copolymers, (ii) their assembly into medium-dependent light-responsive polymersomes, (iii) real-time monitoring of cargo photorelease by cyclic voltammetry, and (iv) their application as an intelligent labeling system in the development of a biosensor. In this context, a new class of multicoordinated and multifunctional random amphiphilic copolymers resulted from functionalizing the poly(ethylene-*alt*-maleic an-hydride) (PEMA) with *p*-aminoazobenzene (*p*-AAB) copolymer and biotin through a one-step nucleophilic substitution reaction. The resultant copolymers were suitable for self-assembly into well-defined nanopolymersomes named $V_{PEMA\text{-}AAB}$ and $V_{PEMA\text{-}AAB\text{-}biotin}$ with the ability to encapsulate hydrophilic and hydrophobic cargo, exhibiting dual responsiveness to light and the nature and composition of the surrounding media. For example, AZO moieties disrupted the fidelity of the nanopolymersomes' interface through photoinduced isomerization, while nanopolymersomes lose structural stability in media containing kosmotropic anions. Accordingly, cargo (photo)release profiles of nanopolymersomes were either intermittent photorelease, with cargo release halting in the dark and resuming when exposed to light in acidic conditions, or continuous cargo release in a more alkaline medium, significantly enhanced by irradiation.

To demonstrate the practical utility of the as-developed nanopolymersome-based cargo-photo release system, quantitative (photo)release of methylene blue (MB) electroactive species was achieved on the fly from $MB_{10\%}$-$V_{PEMA\text{-}AAB}$ using cyclic voltammetry, incorporating horseradish peroxidase (HRP) enzyme into the $V_{PEMA\text{-}AAB\text{-}biotin}$ and demonstrating its application as an intelligent labeling system by optical biosensing of interleukin-6. While the described application utilizing the AZO-based polymersomes designed as a photo-switch smart nanosystem is restricted by UV light excitation source, this research introduced a general synthetic route for modifying the polymersome functional groups right before self-assembly. It opens the path to other potential uses, such as smart delivery systems, nano-reactors, etc., and new visible or near-infrared (NIR) photo-switching AZO derivatives [57,58]**.**

ASSOCIATED CONTENT

Supporting Information

The Supporting Information is available free of charge on the Chemical Engineering Journal Publications website.

^{1}H-NMR and FTIR spectra and assignment, TGA and DTG thermograms, intensity-average D_H distribution and autocorrelation function, UV-vis absorption spectra, TEM micrographs, cyclic voltammograms, calibration curves, XRD patterns, and EDX spectrum are in the supporting information (PDF).

AUTHOR INFORMATION

Corresponding Author

E-mail: grupotandem.nanobioe@udea.edu.co

CRediT authorship contribution statement

Jennifer Quinchia: Conceptualization, methodology, formal analysis, investigation, data curation, writing-original draft. **Andrés F. Cruz-Pacheco:** Conceptualization, investigation, data curation, writing-original draft. **Daniel Ruiz-Molina:** Review & Editing, technical support. **Jahir Orozco:** Conceptualization, formal analysis, writing-review & Editing, supervision, project administration, funding acquisition.

Declaration of competing interest

The authors declare that they have no known competing financial interests or personal relationships that could have appeared to influence the work reported in this paper.

ACKNOWLEDGMENT

The work has been funded by MINCIENCIAS, MINEDUCACIÓN, MINCIT, and ICETEX through the Program Ecosistema Científico Cod. FP44842-211-2018, project number 58536. J.O thanks support from The University of Antioquia and the Max Planck Society through the cooperation agreement 566-1, 2014. In addition, we thank The Ruta N complex and EPM for hosting the Max Planck Tandem Groups. This work was partially supported by grant PID2021-127983OB-C21 financed by MCIN/ AEI/10.13039/501100011033/ and ERDF A Way to Make Europe. We thank Prof. Giuseppe Battaglia and MSc José Muñoz López from the Molecular Bionics Group from the Institute for Bioengineering of Catalonia (IBEC) for the SLS measurements.

REFERENCES

[1] M. Aflori, Smart nanomaterials for biomedical applications—a review, Nanomaterials. 11 (2021) 396. https://doi.org/10.3390/nano11020396.

[2] P. Mena-Giraldo, J. Orozco, Polymeric micro/nanocarriers and motors for cargo transport and phototriggered delivery, Polymers (Basel). 13 (2021) 3920. https://doi.org/10.3390/polym13223920.

[3] P. Mena-Giraldo, S. Pérez-Buitrago, M. Londoño-Berrío, I.C. Ortiz-Trujillo, L.M. Hoyos-Palacio, J. Orozco, Photosensitive nanocarriers for specific delivery of cargo into cells, Sci. Rep. 10 (2020) 1–12. https://doi.org/10.1038/s41598-020-58865-z.

[4] E. Hernández Becerra, J. Quinchia, C. Castro, J. Orozco, Light-Triggered Polymersome-Based Anticancer Therapeutics Delivery, Nanomaterials. 12 (2022) 836. https://doi.org/10.3390/nano12050836.

[5] P. Mena-Giraldo, J. Orozco, Photosensitive Polymeric Janus Micromotor for Enzymatic Activity Protection and Enhanced Substrate Degradation, ACS Appl. Mater. Interfaces. 14 (2022) 5897–5907. https://doi.org/10.1021/acsami.1c14663.

[6] L. Wang, Q. Li, Photochromism into nanosystems: Towards lighting up the future nanoworld, Chem. Soc. Rev. 47 (2018) 1044–1097. https://doi.org/10.1039/c7cs00630f.

[7] H. Dürr, H. Bouas-Laurent, Photochromism: Molecules and Systems, Elsevier, Amsterdam, 2003.

[8] S. Kobayashi, K. Müllen, Encyclopedia of Polymeric Nanomaterials, Springer Berlin Heidelberg, Berlin, Heidelberg, 2015. https://doi.org/10.1007/978-3-642-29648-2-119.

[9] A. Emoto, E. Uchida, T. Fukuda, Optical and physical applications of photocontrollable materials: Azobenzene-containing and liquid crystalline polymers, Polymers (Basel). 4 (2012) 150–186. https://doi.org/10.3390/polym4010150.

[10] H.B. Cheng, S. Zhang, J. Qi, X.J. Liang, J. Yoon, Advances in Application of Azobenzene as a Trigger in Biomedicine: Molecular Design and Spontaneous Assembly, Adv. Mater. 33 (2021) 1–42. https://doi.org/10.1002/adma.202007290.

[11] M. Zheng, J. Yuan, Polymeric nanostructures based on azobenzene and their biomedical applications: synthesis, self-assembly and stimuli-responsiveness, Org.

Biomol. Chem. 20 (2022) 749–767. https://doi.org/10.1039/D1OB01823J.
[12] G.S. Kumar, D.C. Neckers, Photochemistry of Azobenzene-Containing Polymers, Chem. Rev. 89 (1989) 1915–1925. https://doi.org/10.1021/cr00098a012.
[13] H.M.D. Bandara, S.C. Burdette, Photoisomerization in different classes of azobenzene, Chem. Soc. Rev. 41 (2012) 1809–1825. https://doi.org/10.1039/c1cs15179g.
[14] S.L. Oscurato, M. Salvatore, P. Maddalena, A. Ambrosio, From nanoscopic to macroscopic photo-driven motion in azobenzene-containing materials, Nanophotonics. 7 (2018) 1387–1422. https://doi.org/10.1515/nanoph-2018-0040.
[15] E. Rideau, R. Dimova, P. Schwille, F.R. Wurm, K. Landfester, Liposomes and polymersomes: a comparative review towards cell mimicking, Chem. Soc. Rev. 47 (2018) 8572–8610. https://doi.org/10.1039/c8cs00162f.
[16] J. Leong, J.Y. Teo, V.K. Aakalu, Y.Y. Yang, H. Kong, Engineering Polymersomes for Diagnostics and Therapy, Adv. Healthc. Mater. 7 (2018) 1701276. https://doi.org/10.1002/adhm.201701276.
[17] N. Li, Y. Li, X. Wang, Photoresponsive submicron-sized hollow spheres obtained from amphiphilic azobenzene-containing random copolymer, Polymer (Guildf). 53 (2012) 3975–3985. https://doi.org/10.1016/j.polymer.2012.07.001.
[18] S.M. Safar Sajadi, S. Khoee, The simultaneous role of porphyrins' H- and J-aggregates and host–guest chemistry on the fabrication of reversible Dextran-PMMA polymersome, Sci. Rep. 11 (2021) 2832. https://doi.org/10.1038/s41598-021-82256-7.
[19] L. Mora, K.Y. Chumbimuni-Torres, C. Clawson, L. Hernandez, L. Zhang, J. Wang, Real-time electrochemical monitoring of drug release from therapeutic nanoparticles, J. Control. Release. 140 (2009) 69–73. https://doi.org/10.1016/j.jconrel.2009.08.002.
[20] D. Yu, P. Ruan, Z. Meng, J. Zhou, The Structure-Dependent Electric Release and Enhanced Oxidation of Drug in Graphene Oxide-Based Nanocarrier Loaded with Anticancer Herbal Drug Berberine, J. Pharm. Sci. 104 (2015) 2489–2500. https://doi.org/10.1002/jps.24491.
[21] D. Samanta, N. Hosseini-Nassab, R.N. Zare, Electroresponsive nanoparticles for drug delivery on demand, Nanoscale. 8 (2016) 9310–9317.

https://doi.org/10.1039/c6nr01884j.

[22] J.J. Otarola, A.K. Cobo Solis, M.E. Farias, M. Garrido, N. Mariano Correa, P.G. Molina, Piroxicam-loaded nanostructured lipid carriers gel: Design and characterization by square wave voltammetry, Colloids Surfaces A Physicochem. Eng. Asp. 606 (2020) 125396. https://doi.org/10.1016/j.colsurfa.2020.125396.

[23] S. Romanò, A. Angelillo, W. Cimmino, N. Iaccarino, V. Nele, V. Campani, G. De Rosa, S. Cinti, An Electrochemical Strip to Evaluate and to Discriminate Drug Encapsulation in Lipid Nanovectors, Anal. Chem. (2024). https://doi.org/10.1021/acs.analchem.4c01997.

[24] A. Gibalova, L. Kortekaas, J. Simke, B.J. Ravoo, Multi-responsive Electropolymer Surface Coatings Based on Azo Molecular Switches and Carbazoles: Light, pH, and Electrochemical Control of Z → E Isomerization in Thin Films, Chem. - A Eur. J. 29 (2023) 1–9. https://doi.org/10.1002/chem.202302215.

[25] S. Schrader, V. Zauls, B. Dietzel, C. Flueraru, D. Prescher, J. Reiche, H. Motschmann, L. Brehmer, Linear and nonlinear optical properties of Langmuir-Blodgett multilayers from chromophore-containing maleic acid anhydride polymers, Mater. Sci. Eng. C. 8–9 (1999) 527–537. https://doi.org/10.1016/S0928-4931(99)00088-0.

[26] V.A. Vasantha, C. Junhui, Z. Wenguang, A.M. Van Herk, A. Parthiban, Reversible Photo- and Thermoresponsive, Self-Assembling Azobenzene Containing Zwitterionic Polymers, Langmuir. 35 (2019) 1465–1474. https://doi.org/10.1021/acs.langmuir.8b01820.

[27] W. Wang, X. Ji, H. Bin Na, M. Safi, A. Smith, G. Palui, J.M. Perez, H. Mattoussi, Design of a multi-dopamine-modified polymer ligand optimally suited for interfacing magnetic nanoparticles with biological systems, Langmuir. 30 (2014) 6197–6208. https://doi.org/10.1021/la500974r.

[28] Z. Jin, L. Du, C. Zhang, Y. Sugiyama, W. Wang, G. Palui, S. Wang, H. Mattoussi, Modification of Poly(maleic anhydride)-Based Polymers with H_2N-R Nucleophiles: Addition or Substitution Reaction?, Bioconjug. Chem. 30 (2019) 871–880. https://doi.org/10.1021/acs.bioconjchem.9b00008.

[29] B.T. Mai, J.S. Conteh, H. Gavilán, A. Di Girolamo, T. Pellegrino, Clickable Polymer Ligand-Functionalized Iron Oxide Nanocubes: A Promising Nanoplatform for ‘Local

Spots' Magnetically Triggered Drug Release, ACS Appl. Mater. InterfacesMaterials Interfaces. 14 (2022) 48476–48488. https://doi.org/10.1021/acsami.2c14752.

[30] Guan, Y. Ding, S. Lai, X. Yang, J. Wei, J. Zhang, L. Zhang, K. Wang, J. Tong, C. Nonconjugated fluorescent polymer nanoparticles by self-assembly of PIMA-g-β- for live-cell long-term tracking, Carbohydr. Polym. 291 (2022). https://doi.org/10.1016/j.carbpol.2022.119633.

[31] M.H. El-Newehy, H. El-Hamshary, A. Alamri, S.S. Al-Deyab, Synthesis and modification of amine-terminated maleic anhydride-ethylene copolymers by benzaldehyde derivatives: Characterization and antimicrobial properties, Int. J. Polym. Mater. Polym. Biomater. 63 (2014) 563–575. https://doi.org/10.1080/00914037.2013.854228.

[32] Stauch, R. Schubert, G. Savin, W. Burchard, Structure of artificial cytoskeleton containing liposomes in aqueous solution studied by static and dynamic light scattering, Biomacromolecules. 3 (2002) 565–578. https://doi.org/10.1021/bm0200074.

[33] Habel, A. Ogbonna, N. Larsen, S. Cherré, S. Kynde, S.R. Midtgaard, K. Kinoshita, Krabbe, G.V. Jensen, J.S. Hansen, K. Almdal, C. Hèlix-Nielsen, Selecting analytical tools for characterization of polymersomes in aqueous solution, RSC Adv. (2015) 79924–79946. https://doi.org/10.1039/c5ra16403f.

[34] Kang, H. Tang, Z. Zhao, S. Song, Hofmeister Series: Insights of Ion Specificity from Amphiphilic Assembly and Interface Property, ACS Omega. 5 (2020) 6229–

6239. https://doi.org/10.1021/acsomega.0c00237.

[35] Marcus, Effect of ions on the structure of water: structure making and breaking, Chem. Rev. 109 (2009) 1346–1370. https://doi.org/10.1351/PAC-CON-09-07-02.

[36] Hu, Y. Zhang, Z. Xie, X. Jing, A. Bellotti, Z. Gu, Stimuli-Responsive Polymersomes for Biomedical Applications, Biomacromolecules. 18 (2017) 649–673. https://doi.org/10.1021/acs.biomac.6b01704.

[37] R.M. Perera, S. Gupta, T. Li, M. Bleuel, K. Hong, G.J. Schneider, Influence of NaCl shape deformation of polymersomes, Soft Matter. 17 (2021) 4452–4463. https://doi.org/10.1039/d0sm02271c.

[38] Y. Men, W. Li, C. Lebleu, J. Sun, D.A. Wilson, Tailoring Polymersome Shape Using the Hofmeister Effect, Biomacromolecules. (2019). https://doi.org/10.1021/acs.biomac.9b00924.

[39] F. Liu, A. Eisenberg, Preparation and pH Triggered Inversion of Vesicles from Poly(acrylic Acid)-block-Polystyrene-block-Poly(4-vinyl Pyridine), J. Am. Chem. Soc. 125 (2003) 15059–15064. https://doi.org/10.1021/ja038142r.

[40] Y. Geng, F. Ahmed, N. Bhasin, D.E. Discher, Visualizing worm micelle dynamics and phase transitions of a charged diblock copolymer in water, J. Phys. Chem. B. 109 (2005) 3772–3779. https://doi.org/10.1021/jp0459559.

[41] P. Palladino, F. Torrini, S. Scarano, M. Minunni, 3,3′,5,5′-Tetramethylbenzidine As Multi-Colorimetric Indicator of Chlorine in Water in Line With Health Guideline Values, Anal. Bioanal. Chem. 412 (2020) 7861–7869. https://doi.org/10.1007/s00216-020-02918-9.

[42] J.R. Harris, S. De Carlo, Negative Staining and Cryo-negative Staining: Applications in Biology and Medicine, in: Electron Microsc., Humana Press, Totowa, NJ, 2014: pp. 215–258. https://doi.org/10.1007/978-1-62703-776-1.

[43] H. Che, S. Cao, J.C.M. Van Hest, Feedback-Induced temporal control of “breathing” polymersomes to create self-adaptive nanoreactors, J. Am. Chem. Soc. 140 (2018) 5356–5359. https://doi.org/10.1021/jacs.8b02387.

[44] O. Rifaie-Graham, S. Ulrich, N.F.B. Galensowske, S. Balog, M. Chami, D. Rentsch, J.R. Hemmer, J. Read De Alaniz, L.F. Boesel, N. Bruns, Wavelength-Selective Light-Responsive DASA-Functionalized Polymersome Nanoreactors, J. Am. Chem. Soc. 140 (2018) 8027–8036. https://doi.org/10.1021/jacs.8b04511.

[45] Y. Altay, A. Llopis-Lorente, L.K.E.A. Abdelmohsen, J.C.M. Van Hest, Chemical Cascading Between Polymersomal Nanoreactor Populations, Macromol. Chem. Phys. (2022) 2200269. https://doi.org/10.1002/macp.202200269.

[46] M. Haub, T. Günther, M. Bogner, A. Zimmermann, Investigation of focused ion and electron beam platinum carbon nano-tips with transmission electron microscopy for quantum tunneling vacuum gap applications, Appl. Sci. 11 (2021) 11793. https://doi.org/10.3390/app112411793.

[47] M.R. Molla, P. Rangadurai, L. Antony, S. Swaminathan, J.J. De Pablo, S.

Thayumanavan, Dynamic actuation of glassy polymersomes through isomerization of a single azobenzene unit at the block copolymer interface, Nat. Chem. 10 (2018) 659–666. https://doi.org/10.1038/s41557-018-0027-6.

[48] Y. Yao, Y. Yu, X. Wan, D. Yan, Y. Chen, J. Luo, G.J. Vancso, S. Zhang, Azobenzene-Based Cross-Linked Small-Molecule Vesicles for Precise Oxidative Damage Treatments Featuring Controlled and Prompt Molecular Release, Chem. Mater. 33 (2021) 7357–7366. https://doi.org/10.1021/acs.chemmater.1c01860.

[49] T. Sagara, J. Iizuka, K. Niki, Electroreflectance Study of the Redox Reaction of Methylene Blue Adsorbed on a Pyrolytic Graphite Electrode, Langmuir. 8 (1992) 1018–1025. https://doi.org/10.1021/la00039a046.

[50] F.A. Farahani, E. Alipour, R. Mohammadi, M.S. Amini-Fazl, K. Abnous, Development of novel aptasensor for ultra-sensitive detection of myoglobin via electrochemical signal amplification of methylene blue using poly (styrene)-block-poly (acrylic acid) amphiphilic copolymer, Talanta. 237 (2022) 122950. https://doi.org/10.1016/j.talanta.2021.122950.

[51] Y. Zhang, J. Ai, Y. Dong, S. Zhang, Q. Gao, H. Qi, C. Zhang, Z. Cheng, Combining 3D graphene-like screen-printed carbon electrode with methylene blue-loaded liposomal nanoprobes for phospholipase A2 detection, Biosens. Bioelectron. 126 (2019) 255–260. https://doi.org/https://doi.org/10.1016/j.bios.2018.11.004.

[52] Y. Zheng, J. Li, B. Zhou, H. Ian, H. Shao, Advanced sensitivity amplification strategies for voltammetric immunosensors of tumor marker: State of the art, Biosens. Bioelectron. 178 (2021) 113021. https://doi.org/10.1016/j.bios.2021.113021.

[53] C. Lin, Y. Guo, M. Zhao, M. Sun, F. Luo, L. Guo, B. Qiu, Z. Lin, G. Chen, Highly sensitive colorimetric immunosensor for influenza virus H5N1 based on enzyme-encapsulated liposome, Anal. Chim. Acta. 963 (2017) 112–118. https://doi.org/10.1016/j.aca.2017.01.031.

[54] C. Lin, H. Zheng, M. Sun, Y. Guo, F. Luo, L. Guo, B. Qiu, Z. Lin, G. Chen, Highly sensitive colorimetric aptasensor for ochratoxin A detection based on enzyme-encapsulated liposome, Anal. Chim. Acta. 1002 (2018) 90–96. https://doi.org/10.1016/j.aca.2017.11.061.

[55] P. Brož, S.M. Benito, C.L. Saw, P. Burger, H. Heider, M. Pfisterer, S. Marsch, W.

Meier, P. Hunziker, Cell targeting by a generic receptor-targeted polymer nanocontainer platform, J. Control. Release. 102 (2005) 475–488. https://doi.org/10.1016/j.jconrel.2004.10.014.

[56] Y. Cao, M. Zheng, W. Cai, Z. Wang, Enzyme-loaded liposome with biocatalytic precipitation for potentiometric immunoassay of thyroid-stimulating hormone in thyroid carcinoma, Chinese Chem. Lett. 31 (2020) 463–467. https://doi.org/10.1016/j.cclet.2019.06.024.

[57] A.A. Beharry, O. Sadovski, G.A. Woolley, Azobenzene photoswitching without ultraviolet light, J. Am. Chem. Soc. 133 (2011) 19684–19687. https://doi.org/10.1021/ja209239m.

[58] P. Weis, S. Wu, Light-Switchable Azobenzene-Containing Macromolecules: From UV to Near Infrared, Macromol. Commun. (2018) 1700220. Rapid https://doi.org/10.1002/marc.201700220.

Graphical abstract

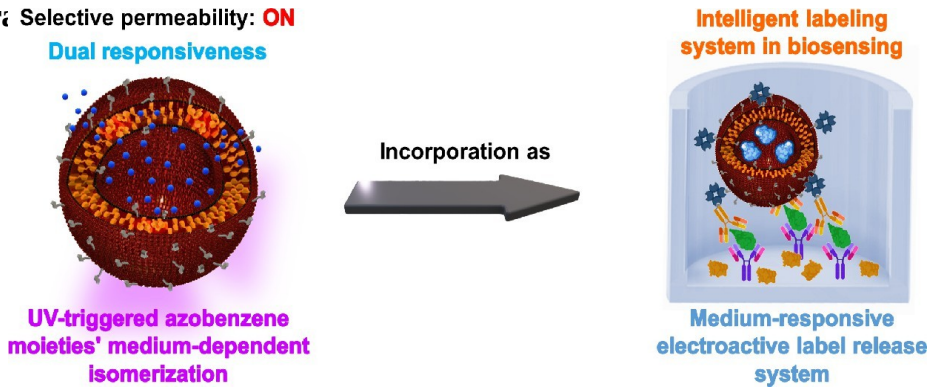

Highlights

- New multicoordinated and multifunctional random amphiphilic copolymers
- Self-assembly of well-organized nanopolymersomes from highly dispersed copolymers
- Ultraviolet-triggered azobenzene moieties' medium-dependent isomerization

- Electroactive species cargo (photo)release monitoring in real-time by CV
- HRP-loaded polymersomes as a medium-responsive electroactive label release system
- Optical biosensing of interleukin-6